AN INVESTIGATION OF STRUCTURAL AND ELECTRONIC PROPERTIES OF ZIRCONOLITE ($CaZrTi_2O_7$) USING DENSITY FUNCTIONAL THEORY

Supported by tetfund

A. Shuaibu[1], S. G. Abdu[1], Y. Aliyu[1,2] and Y. A. Kauru[1]
[1]Department of Physics, Kaduna State University, PMB 2339, Kaduna, Nigeria
[2]Department of Physics, Ahmadu Bello University, Zaria, Kaduna State, Nigeria

Received: September 07, 2020 **Accepted:** November 12, 2020

Abstract: Zirconolite ($CaZrTi_2O_7$) has been acknowledged as the favourable candidate for high level radioactive waste immobilisation due to its effectiveness in aqueous durability, chemical flexibility, waste loading and radiation tolerance. In this study, the structural and electronic properties of zirconolitehave investigated using Density Functional Theory (DFT) within generalized gradient approximation (GGA) as implemented in Quantum ESPRESSO (QE). It was found that the zirconolite structure is stable. The calculated electronic band structure of zirconolite shown along a high symmetry direction and the energy range of band structure is plotted from 0.00 eV to 3.0 eV, the energy separation between the conduction band maximum and valence band minimum occurred at the R_2 and T_2 points, indicating that zirconolite is an indirect band gap material with an approximate value of 2.90 eV energy gap, this value is consistent with previous DFT result but less than the experimental result whichreveals the material's semi-conductivity. The calculated density of the state (DOS) shows the domination of different states in both the valence band and the conduction band while projected density of the state (PDOS) indicates s-orbital of Zr, s-orbital of Ca and p-orbital of Ti atoms are responsible for material properties in the valence band near the Fermi level. The type of chemical bond and charge transfer between the anions and the cations was examined by charge density distribution.

Keywords: DFT, $CaZrTi_2O_7$, zirconolite, immobilisation, electronic properties

Introduction

Nuclear energy has been utilised in different fields, comprising of defence, aerospace, power generation, health care, industry and agriculture (Zhao *et al.,* 2018; Du and Jiang, 2017). The long-lived radioactive waste generated from nuclear fuel cycle has been persistent issue of nuclear energy. Nuclear waste is categorised into low-level waste (LLW), intermediate level waste (ILW) and high-level waste (HLW) based on it is activity and half-lives present (Mulroue and Duffy, 2011). Reprocessing and direct disposal in Geological Disposal Facility (GDF)without reprocessing (Once through nuclear fuel cycle) are the two possible available alternatives for treating spent nuclear fuel (Wattal, 2017).

Reprocessing process involves removal of plutonium (Pu) and uranium (U) for reuse in mixed oxide fuel (MOX) and then fission products (FPs) and minor actinides (MA: Np, Am, Cm) immobilisation in a highly durable glass or ceramic, stored in an interim storage and disposed of in or direct disposal in GDF spent nuclear fuel (Wattal, 2017). Currently around 30% of spent fuel are reprocessed globally generating high quantity of high-level liquid radioactive wastes (HLLW) comprising of long-lived radionuclides with half-lives ranging from thousands to million years (MA: ^{135}Cs, ^{99}T, ^{93}Zr…). MA and Pu are the major causes for long term radiotoxicity of HLW (Ma *et al.,* 2018). Consequently, HLW must be isolated from biosphere for public and environmental protection (Zhao *et al.,*2018).

High-level radionuclides immobilisation within a chemically durable and radiation resistant waste forms has been considered as unique separation method (Ma *et al.,* 2018). A possible effective radionuclides immobilisation that would confine radionuclides migration into the environment via underground water was proposed using multi-barrier concept which entails of wasteform, container, engineered barrier and geological barrier (Zhao *et al.,* 2018). The bubble formation due to hydrogen gas within the cement matrix leads to reduction in mechanical strength. As such a solid matrix of borosilicate glass is used for HLW. The use of ceramics matrices for HLW encapsulation was proposed over borosilicate glasses due to its higher retention of actinides elements in leach tests as well as naturally occurring ceramic materials (Mulroue and Duffy, 2011; Gilbert *et al.,* 2010).

In addition, low thermal stability of glass attributed to its failure in actinides waste disposal (Zhang *et al*., 2019). Alternatively, SYNROC, a synthetic rock which was derived at the Australian Nuclear Science and Technology Organisation (ANSTO) was proposed to replace borosilicate glasses (Mulroue and Duffy, 2011). SYNROC has various compositions designed for each waste form. SYNROC-C derived by Ringwood in 1981 consists of zirconolite ($CaZrTi_2O_7$), pyrochlore ($A_2B_2O_6X$) and hollandite ($BaAl_2Ti_6O_{16}$) compositions for HLW encapsulation (Ringwood *et al.,* 1981).

Zirconolite is the most suitable actinide-bearing phase among synroc minerals (Mulroue and Duffy, 2011), (Zhang *et al.,* 2019). It was preferred due to its efficiency in aqueous durability, chemical flexibility, waste loading and radiation tolerance (Ma *et al.,* 2018; Caurant *et al.,* 2010). Furthermore, zirconolite crystalline structure exists naturally retaining many minor actinides and lanthanides (Lumpkin *et al.,* 2004; Rossell, 1980). It has been used industrially as main hosting phase for intermediate-level waste (Ma *et al.,* 2018).

Furthermore, Zirconolite is derived from anion-deficient fluorite structure with general formula of $CaZr_xTi_{3-x}O_7$ with $0.8 < x < 1.37$ (Begg *et al.,*1998). it also entails of corner-linked layers of TiO_6 octahedra separated disconnected by Ca and Zr planes' atoms. Three lattices of zirconolite were occupied by titanium with two that are octahedrally attached to oxygen while the third is fivefold-coordinated site. The Ca and Zr atoms interlayer are eightfold and sevenfold coordinated to oxygen separately as shown on Fig. 1 (Begg *et al.,*1998). Zirconolite develop five polytypic forms due to its nature of anion-deficient derivative of fluorite structure (Ma *et al.,* 2018) such as zirconolite-2M (monoclinic, C2/c) (Rossell, 1980), zirconolite-4M (monoclinic, C2/c) (Hadley *et al.,* 2005), zirconolite-3T (trigonal), zirconolite-3O (orthorhombic), zirconolite-6T (trigonal) (Coelho *et al.,*1997; Smith and Lumpkin, 1993). Zirconolite-2M is the predominantly studied structure among polytypes for actinides immobilisation, while zirconolite-6T crystal was only detected

intergrown within zirconolite-3T crystal without comprehensive structural information (Smith and Lumpkin, 1993; Ma *et al.*, 2018). Previous studies proposed the construction of these polytypes by stacking hexagonal tungsten bronze (HTB) and Ca/Zr layer in various orientation (Ma *et al.*, 2018).

Ab-initio methods established on typical density functional theory (DFT) offer suitable means for the calculation and characterization of the material's ground-state properties such as atomic configuration and total energies (Abdullahi *et al.*, 2018). The aim of this article is to reveal the structural and electronic properties of Zirconolite ceramic using Density Functional Theory (DFT) within generalized gradient approximation (GGA) implemented in Quantum ESPRESSO (QE).

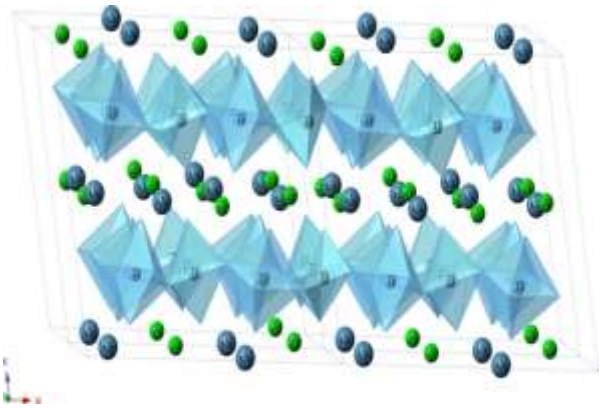

Fig. 1: Schematic illustration of the Zirconolite-2M structure consisting of two HTB and Ca/Zr layers (Ma *et al.*, 2018)

Computational Details

Computational method

The calculations are performed on the $2 \times 2 \times 2$ supercells model of the primitive unit cell of zirconolite ($CaZrTi_2O_7$) based on first principle calculation using density functional theory (DFT). Quantum ESPRESSO simulation package were implemented. The Perdew-Burke-Ernzerhof generalized gradient approximation (PBE-GGA) pseudopotential has been applied for the exchange-correlation potential approximation (Perdew *et al.*,1996). Maxfessel-Paxton smearing method has been employed for integrals. The brillouin zone integration is achieved using Monkhorst-Pack scheme (Monkhorst and Pack, 1976) with $6 \times 6 \times 6$ k-points grids for all materials. Fixed supercell dimensions were used all over the calculations while Broyden-Fletcher-Golfarb-Shannon (BFGS) algorithm was used for total atomic positions relaxation until acting atomic forces are lower than $0.001 eV/Å$.

Results and Discussion

Convergence test

Performing convergence test calculation prior to principal calculation is a basic requirement of any DFT calculation using DFT code. The results presented below represent the convergence testes with respect to plane wave kinetics energy cut-off and k-points mesh for zirconolite crystal ($CaZrTi_2O_7$).

Convergence Test Results of $CaZrTi_2O_7$

Figure 2 shows the convergence result for the zirconolite for the energy cut-off (E-cut (Ry)) with respect to total energy (E_{tot} (Ry)). The graph illustrates the total energy varies considerably with respect kinetic energy cut-off with turning points at 20 Ry and 30 Ry. However, the total energy remains almost constant within the kinetic energy cut-off range of 40-60 Ry (Table 1). This indicates a well-converged kinetic energy cut-off. As such, 40 Ry is taken as an optimized value for the kinetic energy cut-off (E-cut (Ry)) for the zirconolite compound.

Table 1: Convergence test of $CaZrTi_20_7$ total energy with respect to kinetic energy cut-off of the plane wave

S/N	Kinetic energy cut-off (Ry)	Total energy (Ry)
1	10	-2332.42911354
2	20	-2510.07378884
3	30	-2565.77283074
4	40	-2569.44117006
5	50	-2569.57268693
6	60	-2569.60249898

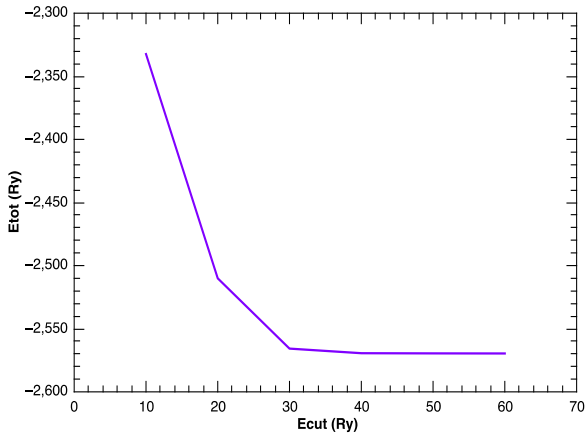

Fig. 2: The convergence of total energy with respect to the kinetic energy cut-off

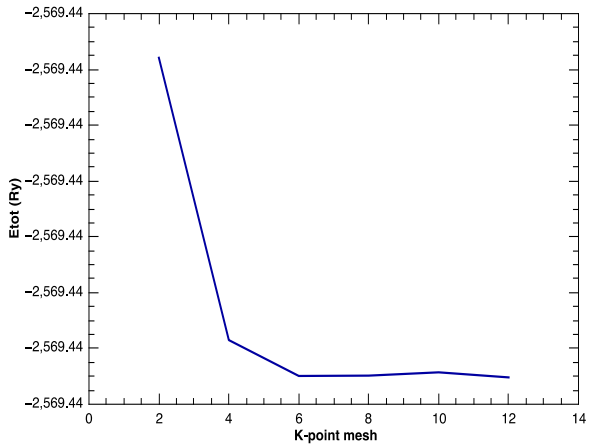

Fig. 3: The convergence of the total energy with respect to the k-points grids

Furthermore, Fig. 3 illustrates the change of thetotal energy with respect to the k-points mesh. the graph shows total energy (E_{tot} (Ry) varies directly with respect to the k-points mesh (Table 2). Nevertheless, the k-point mesh within the range of $2 \times 2 \times 2$ to $12 \times 12 \times 12$ k-points maintain the about the same total energy, which implies less effect on zirconolite's total energy and indicates well-converged k-point. Therefore, $6 \times 6 \times 6$ k-point is regarded as an optimized k-point value for zirconolite compound. Furthermore, the usual method used in DFT calculation for selecting k-points are Monkhorst and pack (Monkhorst and Pack, 1976).

Table 2: Convergence of the total energy with respect to the k-points grids of $CaZrTi_2O_7$

S/N	k-points mesh	Total energy (Ry)
1	$2 \times 2 \times 2$	-2569.44015841
2	$4 \times 4 \times 4$	-2569.44117006
3	$6 \times 6 \times 6$	-2569.44129866
4	$8 \times 8 \times 8$	-2569.44129764
5	$10 \times 10 \times 10$	-2569.44128591
6	$12 \times 12 \times 12$	-2569.44130387

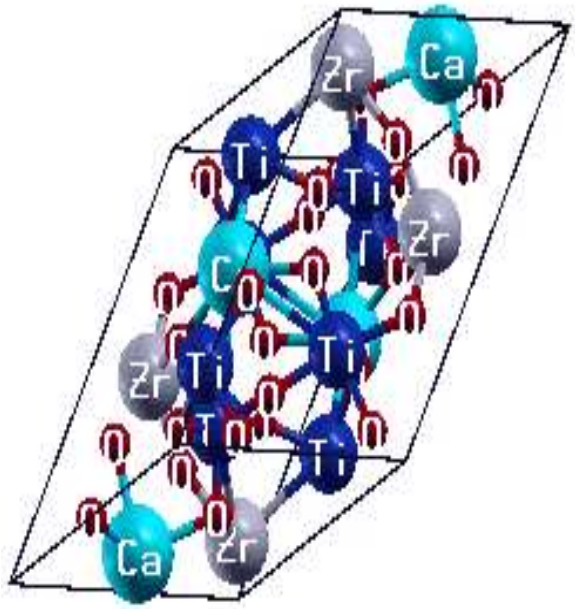

Fig. 4: The bulk structure of simulated. Zirconolite red (small dark) spheres show oxygen ions, grey (large grey spheres show Zr ions) and cyan (large cyan) spheres show Ca ions and blue (large blue) spheres show Ti ions

Structural properties of the zirconolite $CaZrTi_2O_7$

The structural properties of the zirconolite $CaZrTi_2O_7$ with the space group of P1 was simulated as shown on Fig. 4. The zirconolite structure exhibits triclinic geometry with corner-linked layers of TiO_6 octahedra separated by Ca and Zr plane's atoms. Three lattices of zirconolite were occupied by titanium with two that are octahedrally attached to oxygen while the third is fivefold-coordinated site. The Ca and Zr atoms interlayer are eightfold and sevenfold coordinated to oxygen separately (Begg *et al.*,1998). The triclinic crystal structure relates to the primitive unit cell was adopted in this work. The supercell consists of $2 \times 2 \times 2$ supercell (Fig. 4). The optimized crystal parameters of the supercell are $a = 7.286$ Å, $b = 7.315$ Å, $c = 11.477$ Å and $\alpha = 80.977$ °, $\beta = 80.849°$, $\gamma = 60.608°$.

Electronic properties

Electronic properties calculations are crucial in predicting the electronic properties such as band structure, density of state (DOS), projected density of state (PDOS) and charge density distributions of a solids (Afiq *et al.*, 2020). Most of the reported research in the literature on the $CaZrTi_2O_7$ are experimental. A generalized gradient approximation Perdew-Burke-Ernzerhof and generalized gradient approximation (PBE-GGA) were utilized for electronic properties calculation.The calculated electronic band structure of zirconolite compound ($CaZrTi_2O_7$) is shown on Fig. 5 in triclinic phase using PBE-GGA. 11 high symmetry points were selected *(Γ–X |Y–Γ–Z | R_2–Γ–T_2| U_2–Γ–V_2)* (Yoyo *et al.*, 2017; Setyawan and Stefano, 2010) and the band structure energy is plotted between 0.00 eV to 3.0 eV. The Fermi level of the crystal band structure is indicated by the zero (0 eV) on the energy scale. The calculated band structure for $CaZrTiO_7$ within PBE-GGA shows the presence of both Valence Band Maximum (VBM) and Conduction Band Minimum (CBM) at R_2 and T_2 points. The energy separation between VBM and CBM at these symmetry points reveals that the material has indirect band gap. The calculated band gap energy of the material is 2.90 eV, which is 0.70 eV less than the experimentally found value of 3.6 eV (Mulroue and Duffy, 2011; Yuga *et al.*, 2009). In addition, the result also is in agreement with the previously simulated calculated band gap of 2.8. eV as shown on Table 3 (Mulroue *et al.*,2011). This is ascribed to the generally known band gap underestimation generated by erroneous handling of electron-exchange in typical DFT (Idris *et al.*, 2020).

Table 3: Calculated bandgap for $CaZrTi_2O_7$ with previous first principle calculation and experimental data

Method	Bandgap (E/eV)	Difference
Experimental data (Mulroue and Duffy, 2011; Yuga *et al.*, 2009)	3.60	
This work PPE-GGA	2.90	0.70
DFT-PBE (Mulroue and Duffy, 2011)	2.80	0.80

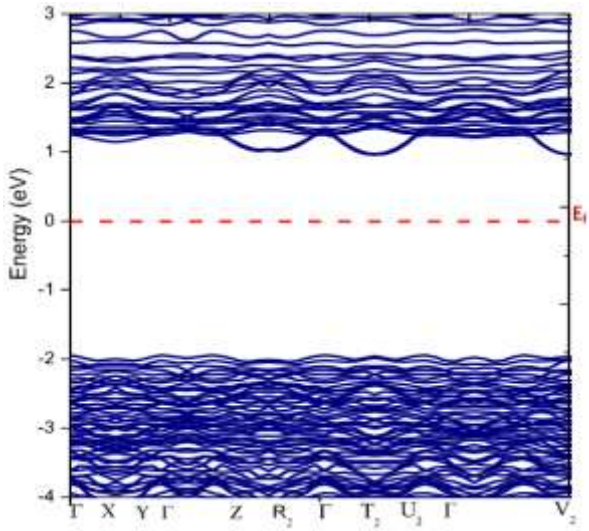

Fig. 5: Calculated band structure of Zirconolite compound ($CaZrTi_2O_7$)

In order to understand the nature of the energy gap more clearly, total density of state (DOS) and projected density of state (PDOS) as well as charge density distribution of zirconolite were studied. Figs. 6 and 7 generally showed the presence of high peaks at the valence band and low peaks at the conduction band. The valence band of zirconolitecomprised of three regions, the lowest occurrence of valence band between -58.2 eV and -40 eV due to the contribution of the Ti-3s, Zr-4s and Ca-3s orbitals, the intermediate occurrence of valence band between -34.5 eV and -191.10 eV which is the highest peak region due to the domination of the Ti-3p, Zr-4p, Ca-3p orbitals with the minor contribution of the Ti-4s, O-2p, Ca-4s, Ca-4p and Zr-5p orbitals and the highest occurrence of valence band which is just below the Fermi level between -6.2 eV and -2.0 eV which

is the lowest peak dominated by O-2p orbital with the minor contribution of O-2s, Ti-3d, Zr-4d and Ca-4s.

Furthermore, the DOS and PDOS (Figs. 6 and 7) are zero between -2 eV and 0.9 eV which implies unavailable states for occupation, as such this can be considered as band gap which is calculated as 2.9 eV. The occupied conduction band between 0.9 eV to 3.9 eV consists of combined hybridization of Ti-3d, O-2s, O-2p. orbitals and minor contribution of Ca-4s, Ca-4p and Zr-4s orbitals.

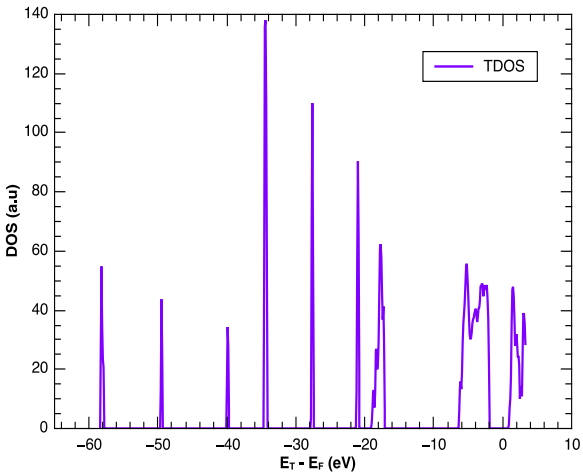

Fig. 6: The total density of states for the zirconolite compound ($CaZrTi_2O_7$)

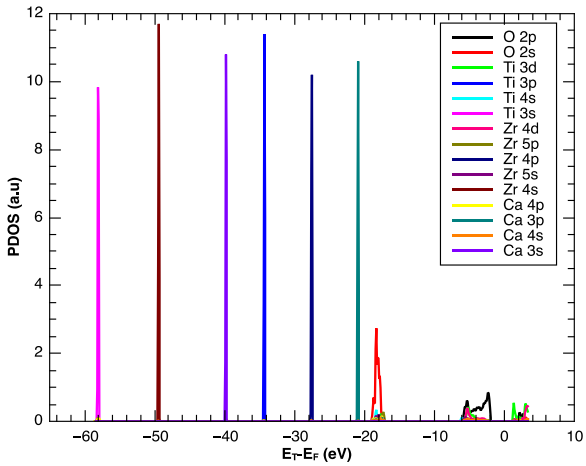

Fig. 7: The projected density of states of the zirconolite compound ($CaZrTi_2O_7$)

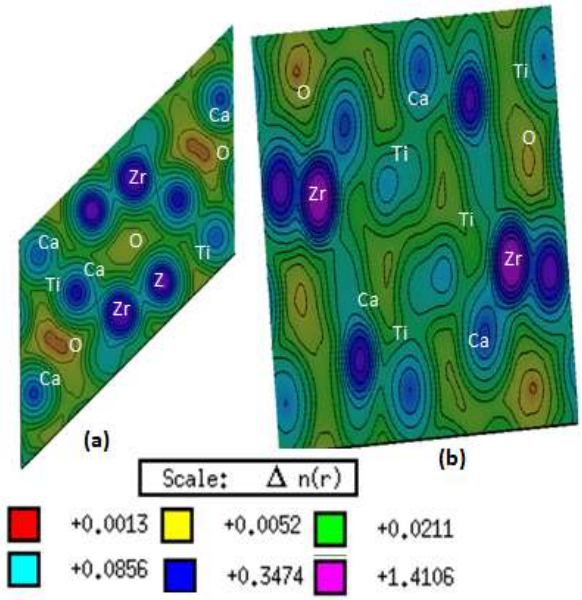

Fig. 8: (a) The side (b) The front view of the charge density plot for the zirconolite ($CaZrTi_2O_7$) The scale n(r) indicating ranges of isodensity values in atomic unit (a.u)

Figure 8 shows that the shape of charge distribution along the cations (Ca^{2+}, Zr^{4+}, Ti^{4+}) are spherical, signifying charge transfer between the atoms. Therefore, the cations make ionic bonding due to transfer of charges to O atoms. The thermometer from Fig. 8 shows that the magenta colour develops the highest charge (+1.4106) which relates to the maximum charge accumulation. Thus, Zirconium (4s) atom has the greatest charge distribution than other atoms. The Oxygen (2s) atom with the red colour has a weaker charge density (+0.0013) while the Titanium has a moderate charge density. This implies that the Zirconium has the smallest ionic radius and greatest charge distribution compared to the rest of the atoms.

Conclusion

The structural and electronic properties of zirconolite, a promising compound and complicated ceramic for high level radioactive waste encapsulation, was investigated using Quantum ESPRESSO code within DFT. A generalized gradient approximation (PBE-GGA) approximation was applied to calculate the total energy. The Structure of the zirconolite $CaZrTi_2O_7$ was found to be stable against decomposition and it is also near the experimental and theoretical calculations. The electronic properties of the material show that the energy separation between the Conduction Band Minimum (CBM) and Valence Band Maximum (VBM) at the R_2 and T_2 points which indicated calculated indirect band gap nature and the band gap value of 2.90 eV. The result is in agreement with the theoretical calculated value and less than the experimental value due to the known concern of DFT. In addition, the density of state (DOS) and projected density of state (PDOS) calculated indicated that the dominations of different states in both the valence band and the conduction band as well as orbital contributions, the peaks predominate in the valence band compared to conduction band. The disposition of chemical bond and charge transfer between the anions and the cations were examined by the charge density distribution calculation which shows the ionic nature of bond and zirconium as the largest charge density.

Acknowledgments
We thank all co-authors for the generous clarifying components and suggestions, which helps considerably in improving this work.

Conflict of Interest
Authors have declared that there is no conflict of interest reported in this work.

References

Abdullahi L, Shaari A & Taura LS 2018. Investigation of excitonic states effects on optoelectronic properties of Sb2Se3 crystal for broadband photo-detector by highly accurate first-principle approach. *Current Applied Physics*, 18: 567-575.

Afiq R, Rashid A, Amiruddin S & Abdullahi L 2020. First-principles study of electronic and optical properties of antimony sulphide thin film. *Optik-Int'l. J. Light and Electron Optics*, 163631.

Begg BD, Vance ER, Hunter BA & Hanna JV 1998. Zirconolite transformation under reducing conditions. *J. Materials Res.*, 13(11): 3181-3190.

Caurant D, Pascal L & Isabelle B 2010. Structural characterisation of Nd-doped Hf-zirconolite Ca1-xNdxHfTi2-XAlxO7 ceramics. *J. Material Sci.*, 407: 88-99.

Coelho AA, Cheary RW & Smith KL 1997. Analysis and structural determination of Nd-substituted zirconolite - 4M. *J. Solid State Chem.*, 346-359.

Du J & Jiang G 2017. Asystematic theoretical study of. UC6: Structure, bonding nature, and spectroscopy. *Inorganic Chemistry*, 13794-13800.

Gilbert M, Davoisine C, Stennett M, Hyatt N, Peng N, Jeynes C & Lee W 2010. Krypton and helium irradiation damage in neodymium-zirconolite. *J. Nuclear Materials*, 221-224.

Hadley JH, Hsu FH, Vance ER, Colella M, Smith KL, Lumpkin G, . . . Begg BD 2005. Cation vacancies in doped zirconolite (CaZrTi2O7). *J. Material Sci.*, 6029-6032.

Idris M, Shaari A, Razali R, Abdullahi L & Ahams ST 2020. DFT+U studies of structure and optoelectronic properties of Fe2SiO4 spinel. *Computational Condensed Matter*, e00460.

Lumpkin G, Smith KL, Giere R & Williams CT 2004. Geochemical behaviour of host phases for actinides and fission products in crystalline ceramic nuclear waste forms. *Geol. Soc. London Special Publication*, 89-111.

Ma S, Shiyin J, Changzhong L, Chengshuai L, Kaima S & Wei H 2018. Effects of ionic radius on phase evolution in Ln-Al co doped Ca1-xLnxZrTi2-xAlxO7 solid solutions. *Ceramics International*, 15124-15132.

Monkhorst HJ & Pack JD 1976. Special points for Brillouin-zone integration. *Physical Review B*, 5188-5192.

Mulroue J & Duffy D 2011. *Ab initio study of the effect of charge localisation on the properties of defects in magnesium oxide and zirconolite*. United Kingdom: University College london.

Mulroue J, Andrew JM & Dorothy M D 2011. Ab inition study of intrinsic defects in zirconolite. *Physical Review B*, 84(9-1): 094118.

Perdew JP, Burke K & Ernzerhof M 1996. Generalized gradient approximation made simple. *Physical Review Letters*, 3865.

Ringwood A, Oversby V, Kesson S, Sinclair W, Ware N, Hibberson W & Major A 1981. Immobilization of high-level nuclear reactor wastes in. SYNROC: A current appraisal. *Nuclear and Chem. Waste Mgt.*, 287-305.

Rossell HJ 1980. Zirconolite-a fluorite-related superstructure. *Nature*, 283: 282-283.

Setyawan W & Stefano C 2010. High-throughput electronic band strucuture calculations: Challenges and tools. *Computational Materials Science*, 49: 299-312.

Smith K & Lumpkin GR 1993. Structural features of zirconolite, hollandide and perovskite, the major waste-bearing phases in synroc, Defects Process. *Solid State Geosci. Appl.*, 401-422.

Wattal P 2017. Back end of Indian nuclear fuel cycle- A road to sustainability. *Progress in Nuclear Energy*, 133-145.

Yoyo H, Giovanni P, Yu K, Fumiyasa O & Isao T 2017. Band structure diagrams based on crystallography. *Computational Materials Science*, 140-184.

Yuga M, Saito K & Kudo A 2009. Nanocrystalline CaZrTi2o7 photocatalyst prepared by a polymerizable complex method in the presence of Cs2CO3 Flux for water splitting. *Chemistry Letters*, 180-181.

Zhang K, Dan Y, Kai X & Haibin Z 2019. Self-propagating synthesis and characterizaion studies of Gd-Bbearing Hf-zirconolite ceramic waste forms. *Materials*, 1-9.

Zhao X, Yuxiang L, Yuancheng T, Lang W, Peng B, Lili W & Shanlin W 2018. The structure, sintering process, and chemical durability of Ce0.5 Gd0.5PO4 ceramics. *Ceramics International*, 44: 19718-19724.